

Article

Transmission of High Frequency Vibrations in Rotating Systems. Application to Cavitation Detection in Hydraulic Turbines

David Valentín * , Alexandre Presas, Mònica Egusquiza , Carme Valero and Eduard Egusquiza

Center for Industrial Diagnostics and Fluid Dynamics (CDIF), Polytechnic University of Catalonia (UPC), Av. Diagonal, 647, ETSEIB, 08028 Barcelona, Spain; alexandre.presas@upc.edu (A.P.); monica.egusquiza@upc.edu (M.E.); m.del.carmen.valero@upc.edu (C.V.); eduard.egusquiza@upc.edu (E.E.)

* Correspondence: david.valentin@upc.edu; Tel.: +34-934-017-132

Received: 21 December 2017; Accepted: 13 March 2018; Published: 16 March 2018

Abstract: One of the main causes of damage in hydraulic turbines is cavitation. While not all cavitation appearing in a turbine is of a destructive type, erosive cavitation can severely affect the structure, thus increasing maintenance costs and reducing the remaining useful life of the machine. Of all types of cavitation, the maximum erosion occurs when clouds of bubbles collapse on the runner surface (cloud cavitation). When this occurs it is associated with a substantial increase in noise, and vibrations that are propagated everywhere throughout the machine. The generation of these cavitation clouds may occur naturally or it may be the response to a periodic pressure fluctuation, like the rotor/stator interaction in a hydraulic turbine. Erosive bubble cavitation generates high-frequency vibrations that are modulated by the shedding frequency. Therefore, the methods for the detection of erosive cavitation in hydraulic turbines are based on the measurement and demodulation of high-frequency vibrations. In this paper, the feasibility of detecting erosive cavitation in hydraulic turbines is investigated experimentally in a rotating disk system, which represents a simplified hydraulic turbine structure. The test rig used consists of a rotating disk submerged in a tank of water and confined with nearby axial and radial rigid surfaces. The excitation patterns produced by cloud cavitation are reproduced with a PZT (piezoelectric patch) located on the disk. These patterns include pseudo-random excitations of different frequency bands modulated by one low carrier frequency, which model the erosive cavitation characteristics. Different types of sensors have been placed in the stationary and in the rotating parts (accelerometers, acoustic emission (AE), and a microphone) in order to detect the excitation pattern. The results obtained for all the sensors tested have been compared in detail for the different excitation patterns applied to the disk. With this information, the best location and type of sensor to detect the different excitations have been identified. This study permits improving the actual technique of detecting erosive cavitation in hydraulic turbines and, therefore, to avoid operation under these circumstances.

Keywords: erosive cavitation; hydraulic turbine; acoustic emission; high frequency; vibration

1. Introduction

Nowadays, hydropower plays an important role in the energy market since it is the only renewable source which is able to compensate for the non-constant energy production of wind or solar power [1–3]. This means that hydro units regulate their power depending on the other renewable sources' production to ensure the stability of the grid and to satisfy the energy demand. However, when hydraulic turbines regulate their power below and above their best efficiency point (BEP), they present different dynamic problems [4–7] which affect the useful life of the mechanical parts of the turbine.

One of the most important problems that always appear in hydraulic turbines is cavitation [8,9]. Cavitation is the formation of vapor cavities in a liquid due to rapid changes in pressure [10]. These cavities can grow, collapsing implosively and emitting large-amplitude shock-waves [11]. This cavitation phenomenon is very important in Francis or reversible pump turbines [8], since their runners are designed to have the maximum efficiency for a given head and flow rate, hence, cavitation appears out of this design point. In Kaplan turbines, cavitation is less likely to occur because they can regulate the angle of their runner blades depending on the head and the flow rate, ensuring a high performance in the whole operating range. The cavitation phenomenon in hydraulic turbines has been studied for many years, especially in laboratory models [12–16].

Different types of cavitation can appear in hydraulic turbines [8,9]. The most important are: leading edge cavitation ((1) in Figure 1), travelling bubbles cavitation ((2) in Figure 1), draft tube swirl ((3) in Figure 1), inter-blade vortex cavitation ((4) in Figure 1), von Karman vortex cavitation ((5) in Figure 1), and tip vortex cavitation (only in Kaplan turbines). Of all types of cavitation, the maximum erosion occurs when clouds of bubbles collapse on the runner surface (cloud cavitation). The generation of these cavitation clouds may occur naturally or it may be the response to a periodic pressure fluctuation like the RSI (rotor stator interaction) in the hydraulic turbine.

The cavitation phenomenon may be different in a real prototype than in the laboratory model because it depends on the operating conditions, therefore, its detection on-site in the power plant is necessary [17,18]. In the past, different studies [9,17–24] were published about the experimental detection of cavitation in hydraulic turbine prototypes. The idea was to detect the shockwaves generated by the collapse of the cavitating bubbles, which are transmitted through the hydraulic turbine structure, by means of analyzing high-frequency vibrations. To do so, accelerometers and acoustic emission (AE) sensors were placed in different parts of the machine. The advantages and drawbacks of every location tested are summarized in the following points:

- Detection with accelerometers in the guide vanes [9,17,19,20,22]: It is a direct measurement but it is only useful for entrance cavitation. It is difficult to separate from erosive and non-erosive cavitation.
- Detection with accelerometers and AE sensors in the turbine bearing [9,17,22]: Only erosive cavitation is detected, but it is an indirect measurement and the transmission characteristics from the runner to the bearing are unknown and filtered.
- Detection with accelerometers in the draft tube [17,22]: Only for draft tube swirl cavitation. It is non-representative of the erosion suffered by the runner.
- Detection with accelerometers in the shaft [21]: Direct path from the runner, but more complicated measurement with the possibility of having also generator excitations.

Two different high-frequency analysis techniques were used to detect erosive cavitation in the previous studies: analyzing the RMS (root mean square) value at high-frequency bands (over 10 kHz) and applying amplitude demodulation techniques, such as the Hilbert transform [25], to obtain the low-frequency oscillation of the cavitation cloud. Figure 1 shows an example of a prototype Francis turbine analyzed with the aforementioned technique. In this case, the power spectrum and amplitude demodulation of a high-frequency band (10–15 kHz) are shown for an accelerometer located in the turbine bearing. Three different operating conditions were analyzed: 70%, 85%, and 100% of the guide vane opening or the maximum power. It is observed that the amplitudes of the spectrum are higher for the 100% of the maximum power and lower for the 70% operating condition. Moreover, the main frequencies related with the rotating speed, RSI, and their harmonics are present when demodulating the signal for the case of 100% of the maximum power, whereas they are not seen in the 70% operating condition. After several hours of operation at 100% of maximum power, severe erosion damage was found in the blades, which was associated with unstable inlet leading edge cavitation.

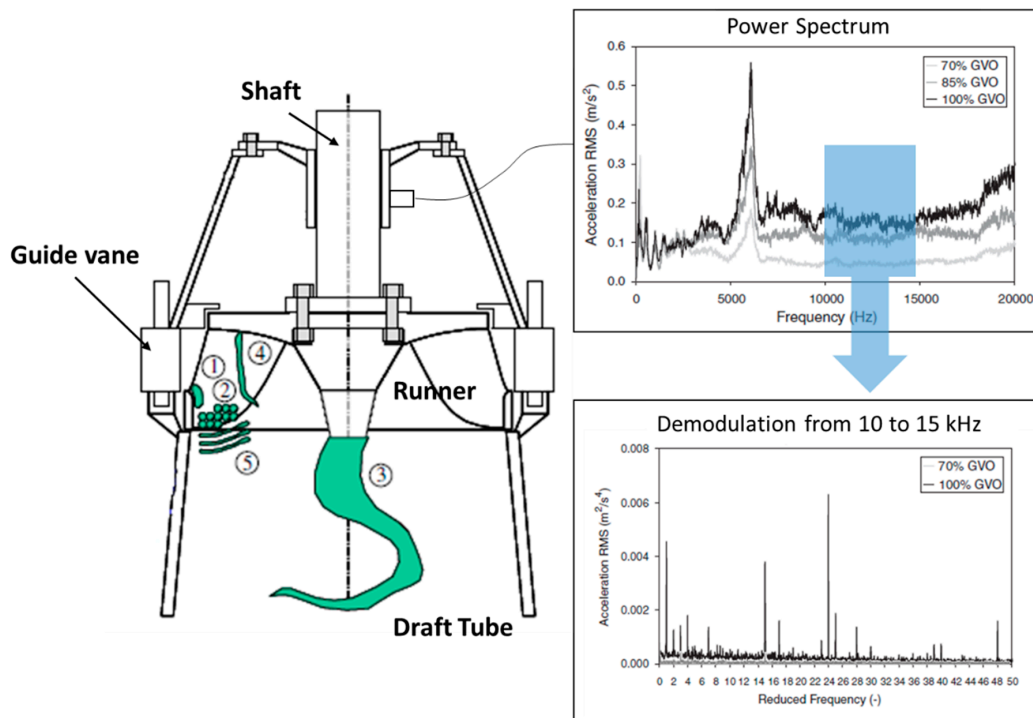


Figure 1. Sketch of a Francis turbine runner showing different types of cavitation and the current method to detect cavitation. The typical cavitation zones are highlighted in green. Adapted with permission from [9], Elsevier, 2006.

Therefore, it seems that the power spectrum amplitude increases and that different peaks appear in the demodulation of the high-frequency bands when erosive cavitation is present in comparison with the non-cavitation case. However, there are still some problems to be solved with this method:

- The transmission path from the runner to the measuring position can only be known in air (the runner could be impacted during an overhaul [17]) but not in water and under operation.
- No correlation between existing cavitation and the measured signals can be obtained: the cavitation cannot be visualized in the prototype [25].
- The excitation characteristics of the cavitation are an unknown.
- It is not clear which high-frequency bands have to be used for every sensor for the analysis.

In this paper, all of these uncertainties are studied using an experimental test rig. The test rig consists of a rotating disk submerged and confined in water. The disk has been instrumented with a PZT (piezoelectric patch) [26–30] and different sensors (accelerometers, AE, and a microphone) have been located in the rotating and stationary parts of the test rig. In that way, the transmission of different excitation patterns simulating cavitation to the different parts of the test rig can be studied in detail. Therefore, since the excitation is completely known, the best transmission path from the excitation to the measuring point can be obtained, as well as the best sensor for its detection. The results obtained in this study permit improving the current methods to detect and monitor [20,31,32] erosive cavitation in hydraulic turbines.

2. Experimental Investigation

The experimental investigation carried out in a laboratory test rig is explained in this section. First, the test rig used is described, then the instruments used are listed and, finally, all the experimental tests conducted are explained.

2.1. Test Rig Description

The test rig used in this paper consists of a rotating disk submerged and confined in water (see Figure 2). The disk is made of stainless steel and it rotates at $f_f = 4.1$ Hz by means of a transmission belt driven by a motor (Mavilor MLV-072) (Mavilor Motors S.A., Santa Perpètua de Mogoda, Spain), which rotates five times faster than the disk (20.5 Hz). The rotating speed is controlled and stabilized with a computer. The excitation and response signals are transmitted from the rotating to the stationary frame through a Michigan S10slip ring. This system is mounted at the tip of the shaft. This test rig has been used in previous studies to analyze the dynamic behavior of the submerged disk-like structures [26,28,29,33–35].

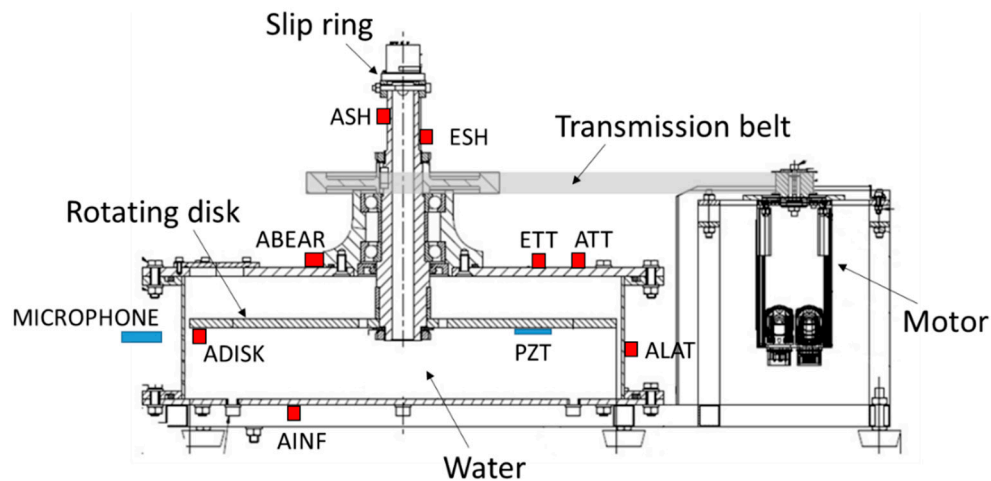


Figure 2. Sketch of the experimental test rig and the sensors installed. ADISK, accelerometer in the disk; AINF, accelerometer in the inferior cover; ABEAR, accelerometer in the bearing; ASH, accelerometer in the shaft; ESH, acoustic emission sensor in the shaft; ETT, acoustic emission sensor in the superior cover; ATT, accelerometer in the superior cover; ALAT, accelerometer in the lateral cover.

2.2. Instrumentation

The disk was instrumented with a PZT (piezoelectric patch) (PI-876A12) glued to the disk with an epoxy component, LOCTITE 454 (Loctite, Hartford, CT, USA). This PZT was used to excite the disk at the desired frequency bands. The PZT works in a range of -100 V to 250 V. For the signal generation, a NI-9263 (National Instruments, Austin, TX, USA) module was used. This module could generate four independent analog outputs with an amplitude of -10 V to 10 V. With an OEM-835 (OEM Systemas Company, Reno, NV, USA) amplifier the analog signal was amplified by 25, so the sent signal to the patch had the desired level. Additionally, a signal to monitor the excitation was sent to the data acquisition system.

To measure the excitation and response of the rotating structures, the disk was instrumented with a miniature and submergible accelerometer (ADISK in Figure 2) (Dytran 3006-A, sensitivity: 100 mV/g) and the shaft with another accelerometer (ASH in Figure 2) (MMF Type KS91B, sensitivity: 10 mV/g) and an AE sensor (ESH in Figure 2) (Brüel and Kjaer Type 8313) (Brüel & Kjaer, Naerum, Denmark).

Moreover, different sensors were located in the stationary parts of the test rig: one accelerometer in the upper cover (ATT in Figure 2) (Kistler 8752A50, sensitivity: 100 mV/g) (Kistler, Winterthur, Switzerland), one in the lower cover (AINF in Figure 2) (MMF Type KS91B, sensitivity: 10 mV/g) (Metra Mess-und Frequenztechnik, Radebeul, Germany), one in the side cover (ALAT in Figure 2) (Dytran 3006-A, sensitivity: 100 mV/g) (Dytran Instruments Inc, Chatsworth, CA, USA) and another one in the bearing (ABEAR in Figure 2) (Dytran 3006-A, sensitivity: 100 mV/g). An AE sensor (Brüel and Kjaer Type 8313) (Brüel & Kjaer, Naerum, Denmark) was also installed in the upper cover (ETT in Figure 2), as well as a microphone (Brüel and Kjaer Type 4957) near the test rig.

The signals were acquired using an acquisition system (Bruel and Kjaer Type 3038) module. The acquisition frequency was set to 25.6 kHz.

2.3. Tests Conducted

In order to represent in the present test rig the typical excitation of erosive cavitation in hydraulic turbines, different excitation patterns were applied to the disk using the PZT. In this case, a pseudorandom excitation in three different ranges of frequency was selected [36]: in the band 1–2 kHz (PS1), in the band 10–11 kHz (PS2), and in the band 20–21 kHz (PS3). Moreover, each one of these pseudorandom excitations was multiplied by a given low-frequency value in order to represent the low-frequency hydraulic phenomena in hydraulic machines. The low frequencies selected were $f_1 = 22.1$ Hz (see Equation (1)), which represents the RSI in the hydraulic turbine, and $f_2 = 1.4$ Hz (see Equation (2)) which represents the vortex rope phenomenon. These values were selected of the same order of those that usually appear in hydraulic turbines, and non-multiple or harmonics of the rotating frequency of the disk. For every pseudorandom excitation, three different tests were conducted: one with only the pseudorandom excitation, one with the pseudorandom excitation and the f_1 , and another one with the pseudorandom excitation and the f_1 and f_2 frequencies (see Table 1 and Figure 3):

$$Envelope1 = \cos(\pi \cdot f_1 \cdot t) \tag{1}$$

$$Envelope2 = \cos(\pi \cdot f_2 \cdot t + \theta) \tag{2}$$

where θ is an arbitrary phase between *Envelope1* and *Envelope2*.

Table 1. Excitation patterns applied to the disk using the PZT (piezoelectric patch).

Excitation Name	Excitation Characteristics
Exc-1-2kHz-0	PS1
Exc2-1-2kHz-1	PS1*Envelope1
Exc3-1-2kHz-2	PS1*Envelope1*Envelope2
Exc-10-11kHz-0	PS2
Exc-10-11kHz-1	PS2*Envelope1
Exc-10-11kHz-2	PS2*Envelope1*Envelope2
Exc-20-21kHz-0	PS3
Exc-20-21kHz-1	PS3*Envelope1
Exc-20-21kHz-2	PS3*Envelope1*Envelope2

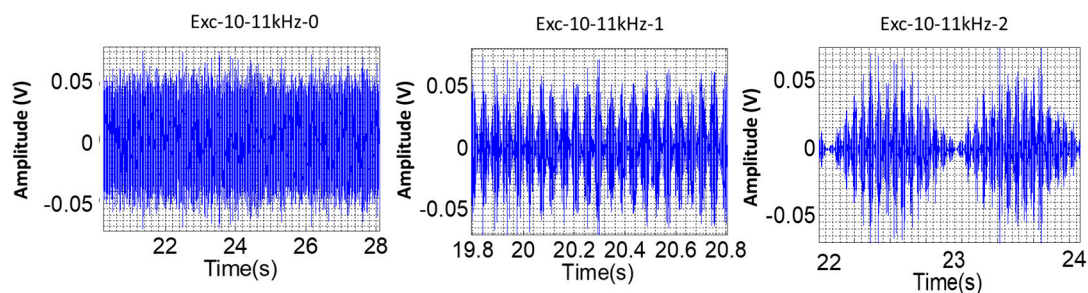


Figure 3. Example of the different excitations used.

Therefore, a total of nine different types of excitations were applied to the disk (see Table 1). These nine excitations were applied to four different configurations: (1) the disk in air without rotation; (2) the disk in water without rotation; (3) the disk in air with rotation ($f_f = 4.1$ Hz); and (4) the disk in water with rotation ($f_f = 4.1$ Hz). In this way, the influence of the water and the rotation could be evaluated for the different excitations applied.

2.4. Signal Analysis

To analyze the signals acquired during the different tests, three different signal analysis methods were applied: coherence between the sensor and the PZT, *FRF* (frequency response function) between the sensor and the PZT and amplitude demodulation analysis to every sensor signal. These methods are explained in detail in the following sections.

2.4.1. Coherence

The coherence between two signals $x(t)$ and $y(t)$ is defined by Equation (3) [36], where $S_{xy}(f)$ is the cross-spectral density of the signal and $S_{xx}(f)$ and $S_{yy}(f)$ are the power spectral density functions of $x(t)$ and $y(t)$, respectively. f is frequency and t is time:

$$Coherence_{xy} = \frac{|S_{xy}(f)|^2}{S_{xx}(f) \cdot S_{yy}(f)} \quad (3)$$

In this case, $x(t)$ is any of the sensor signals and $y(t)$ the excitation signal sent to the PZT. If this value is close to 1, both signals are coherent, which means that the signals acquired by the sensors are caused by the excitation of the PZT. A good coherence between the sensor and the PZT indicates that the transmission path is good. However, if the coherence is close to 0, it means that there is no linear causality effect between the sensor and the excitation signal and, therefore, in this case, it is not useful for the detection of erosive cavitation.

2.4.2. Frequency Response Function (*FRF*)

The *FRF* between two signals $x(t)$ and $y(t)$ is defined as in Equation (4) (also known as FRF_{H1} [36]), where $X(f)$ and $Y(f)$ are $x(t)$ and $y(t)$ in the frequency domain. Again, in this case, $x(t)$ is any of the sensors signal and $y(t)$ the excitation signal sent to the PZT:

$$FRF_{H1} = \frac{X(f) \cdot Y^*(f)}{Y(f) \cdot Y^*(f)} \quad (4)$$

A *FRF* constant along the frequency band studied means that the excitation and the response are totally proportional, whereas a non-constant *FRF* gives the response of the structure due to the excitation. To detect erosive cavitation, it is convenient to have a constant *FRF* along the frequency band, which means that the sensor is directly detecting the excitation and not the structural response due to that excitation.

2.4.3. Amplitude Demodulation Analysis

The demodulation procedure starts filtering the time domain signal in the frequency range studied to remove the low-frequency and high-frequency content outside the frequency range. Then the envelope of the filtered signal is computed using an algorithm based on the Hilbert transform (*Hi*) [9]. Mathematically, the Hilbert transform of a time signal $x(t)$ is defined as in Equation (5):

$$Hi(x(t)) = \frac{1}{\pi} \int_{-\infty}^{\infty} x(\tau) \frac{1}{t - \tau} d\tau \quad (5)$$

The envelope is obtained by forming the complex analytical signal $\tilde{x}(t)$, which is the sum of the time signal $x(t)$ (real part) and the Hilbert transform of $x(t)$ (Equation (5)) (imaginary part):

$$\tilde{x}(t) = x(t) + jHi(x(t)) \quad (6)$$

The analysis of the resulting envelope in Equation (6) in the frequency domain permits identifying the modulating frequencies inside the high-frequency band selected for the study. In this case,

after applying this analysis to the signals acquired by every sensor, it is desired to obtain the rotating frequency (f_f) or the modulating frequencies $f_1 = 22.1$ Hz and $f_2 = 1.4$ Hz depending on the case. The amplitude of the frequencies obtained after applying this analysis can be compared for all the sensors to determine the best sensor to detect erosive cavitation.

3. Results and Discussion

The results obtained for every configuration tested are presented in this section. First, the coherence between the sensors and the PZT is shown and commented. Then the FRF between the different sensors and the PZT is presented and, finally, the amplitude demodulation analysis for the different sensors is discussed.

3.1. Coherence

The coherence between the sensors and the PZT was computed for all the configurations tested. Figure 4 shows the coherence for the sensors installed in the rotating frame and for the three different excitation frequency bands while the disk was standing in air and in water (no rotation). It is seen that coherence is very good for the accelerometer located in the disk (ADISK) and for the AE sensor located in the shaft (ESH) for all the frequency bands, and in air and in water. The points with minimum coherence correspond to antiresonances of the disk [36], so they can be neglected. However, the accelerometer located in the shaft (ASH) presents different results for the lower frequency band (1–2 kHz), where the response of the structure dominates and, therefore, it is not coherent in this zone. For the higher frequency band (20–21 kHz) this accelerometer is coherent both in air and in water.

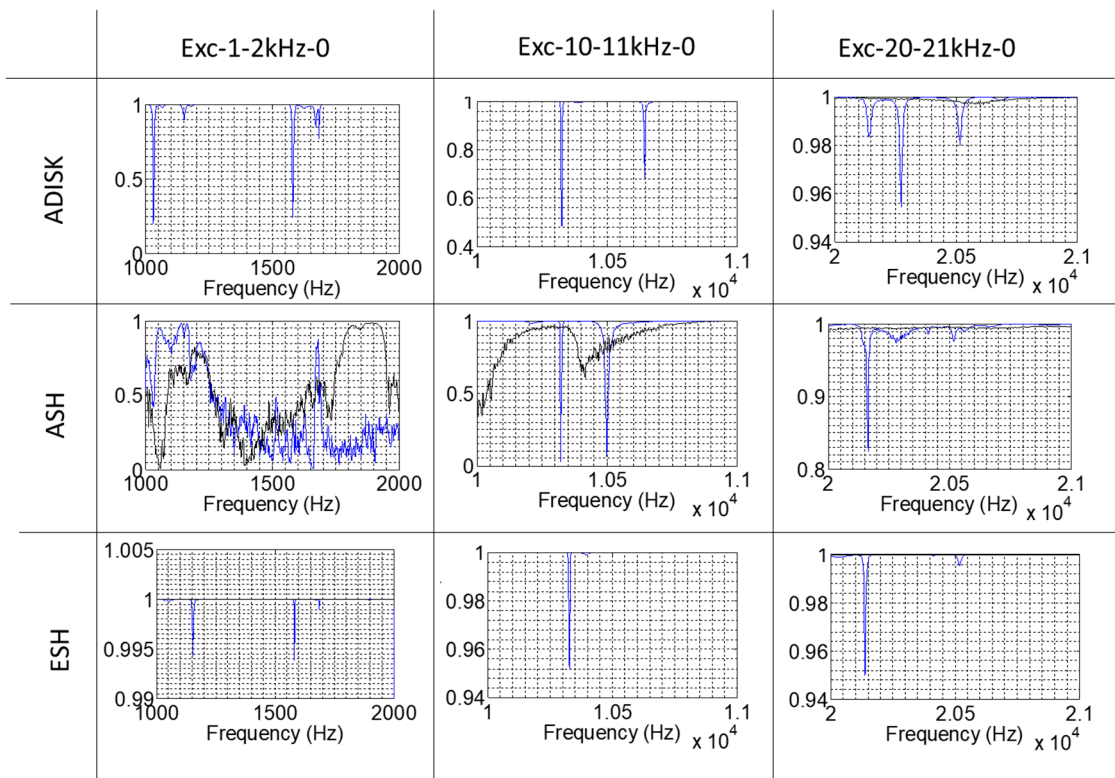


Figure 4. Coherence between the sensors of the rotating frame with respect to the PZT. The blue line is the “in air” configuration, and the black line is the “in water” configuration. Non-rotating case.

Nevertheless, the results of the sensors installed in the stationary parts of the test rig present different results (see Figure 5). The accelerometer in the bearing (ABEAR) shows similar results than the one located in the shaft, so it is thought that both are measuring the same kind of information but in

a different reference frame. The other sensors present better coherence when the disk is submerged in water than in air. This means that the vibration of the disk is mainly transmitted to the stationary parts through the water, and that the mechanical transmission from the disk to the stationary parts is poor. The AE sensor has a good coherence for all the frequency bands with the disk in the water, whereas the microphone better detects the disk vibration for the middle frequency band tested (10–11 kHz), also with the disk in water. The accelerometer located in the lower casing presents only good coherence for the higher frequency band (20–21 kHz) and again only with the disk submerged in water.

Figures 4 and 5 show the coherence for different excitation bands and sensors, in air and in water in the non-rotating case. The same kind of analysis was performed with the disk rotating at 4.1 Hz and the results obtained were almost the same.

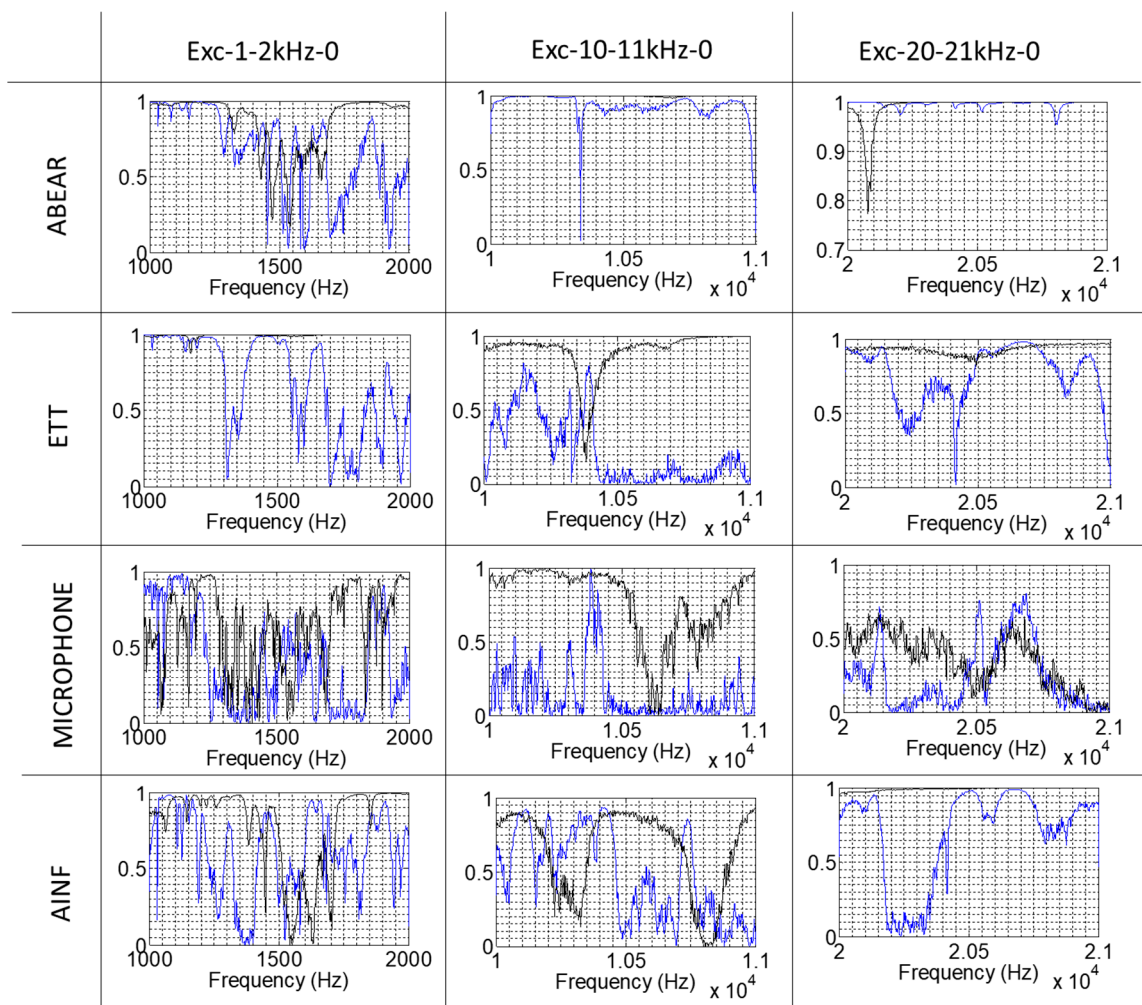


Figure 5. Coherence between the sensors of the stationary frame with respect to the PZT. The blue line is the “in air” configuration, and the black line is the “in water” configuration. Non-rotating case.

3.2. FRF

The frequency response function was computed for those sensors where the coherence was higher, both in air and in water configurations. Those sensors are the ones located in the rotating frame (ADISK, ASH, and ESH). Figure 6 shows the FRF of these three sensors for the excitation “Exc-20-21kHz-0”. It is observed that the FRF in air for the three sensors is not completely constant, the accelerometers being the ones that better detect the structural response. In water, the accelerometer in the disk (ADISK) and the AE sensor in the shaft (ESH) present a constant FRF, whereas the accelerometer in the shaft (ASH) detects some structural response. Moreover, the phase is also constant for the AE sensor. This means

that this sensor receives the propagation of the excitation with no relevant interference from the dynamic behavior of the mechanical system in the excited frequency range. This is an important conclusion, because it means that, in comparison with the accelerometer in the shaft, an AE sensor can better detect the excitation and it eliminates the structural response of the shaft. The same results are obtained for the other frequency bands tested and for the AE sensor in the shaft.

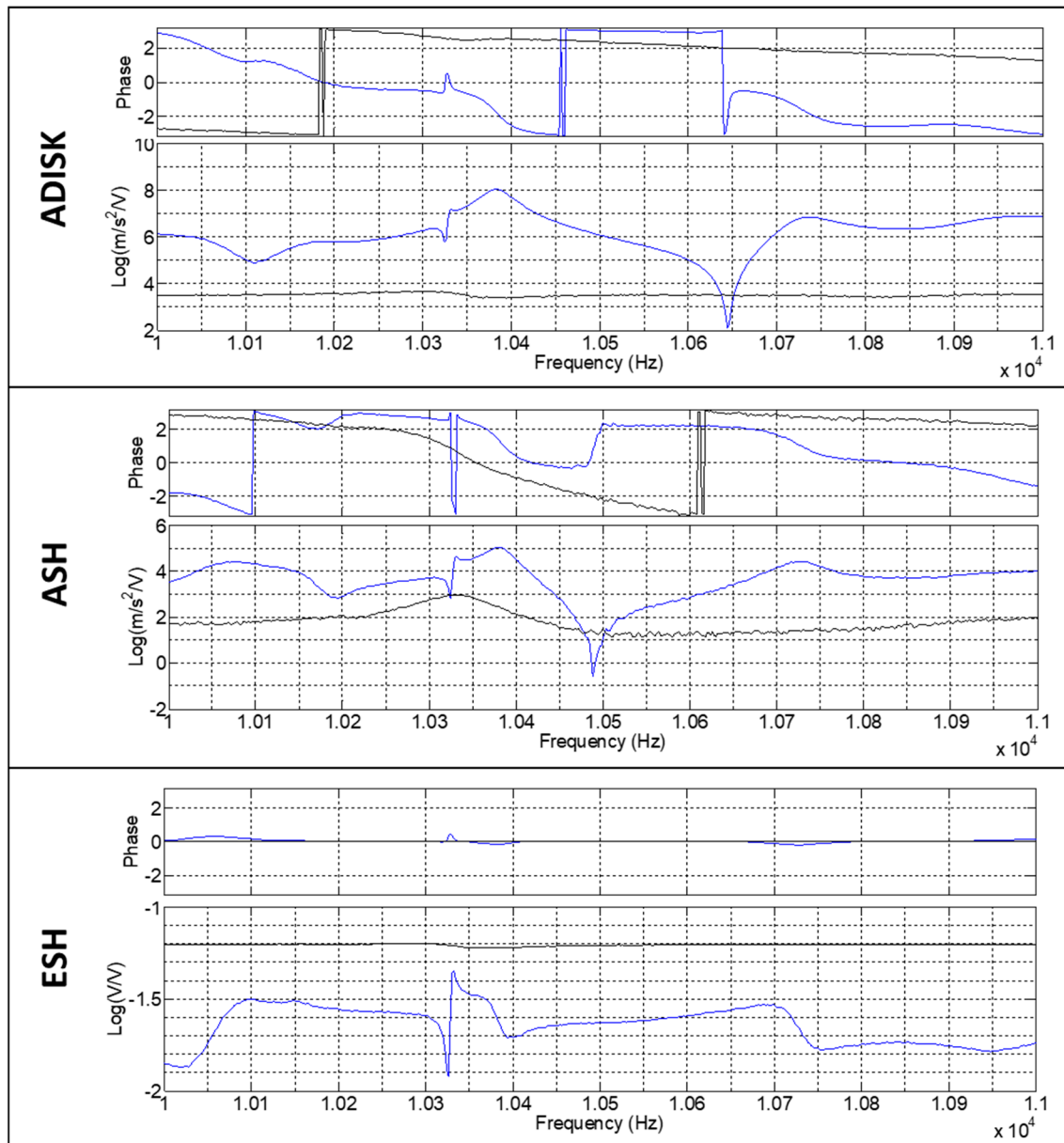


Figure 6. FRF between the sensors in the rotating frame and the PZT for the excitation in the band of 10–11 kHz. The blue line is the “in air” configuration, and the black line is the “in water” configuration. Rotating case ($f_i = 4.1$ Hz).

3.3. Amplitude Demodulation Analysis

An amplitude demodulation analysis was also performed for all the configurations tested. First, the results without modulating frequencies are shown, then the results with one modulating frequency and, finally, the ones with two modulating frequencies.

3.3.1. Without Modulating Frequencies

The results presented in this section are the ones obtained with the excitations called “Exc-1-2kHz-0”, “Exc-10-11kHz-0”, and “Exc-20-21kHz-0” in Table 1. Without any modulating frequencies and only the pseudorandom excitation, after an amplitude demodulation analysis, the only frequency expected to be found is the rotating frequency (f_f) for those cases under rotation in case there is a misalignment in the shaft.

Figure 7 shows this amplitude demodulation analysis for the sensors installed in the rotating frame. It is observed that, for the accelerometer in the shaft (ASH), the rotating frequency is clearly seen for both cases in air and in water, and with greater amplitude in the case of the high-frequency band. The accelerometer in the disk (ADISK) also sees this rotating frequency, but only in the case of the water, where probably the misalignment of the rotating structures is higher. However, the AE sensor located in the shaft (ESH) does not capture this rotating frequency for any of the excitation bands tested. This is another proof that this sensor is not detecting the structural response of the shaft, but it is detecting only the excitation by the transmission of acoustic waves through the structure.

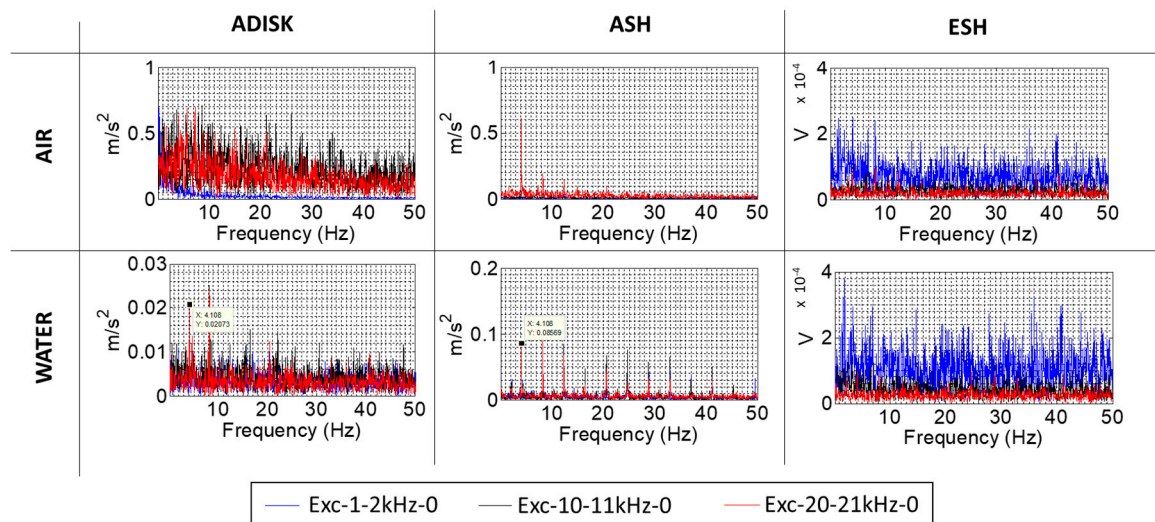


Figure 7. Amplitude demodulation for the sensors on the rotating frame and the excitation without any modulating frequencies. Rotating case ($f_f = 4.1$ Hz).

The results for the stationary sensors are shown in Figure 8. The accelerometer located in the bearing (ABEAR) presents similar results than the one located in the shaft (ASH in Figure 7): it detects the rotating frequency and its harmonics, especially in the high-frequency band (20–21 kHz). However, the rest of sensors from the stationary frame also detect the rotating frequency of the motor (20.5 Hz), its harmonics, and its subharmonics. This is because the vibration of the motor at its rotating frequency is also transmitted through the air and through the support, which is the same piece as the rest of the casing. Therefore, stationary sensors, especially the microphone and the AE sensors in the casing, in this case, are also affected by the motor vibration and not only by the vibration of the rotating part. This is a particular situation in this test rig, but it has to be considered for the analysis of the results. Even so, the accelerometer located in the casing (ATT) is able to detect the rotating frequency of the disk in the case of water for the excitation of 10–11 kHz, where the transmission is better through the liquid, as commented in Section 3.1.

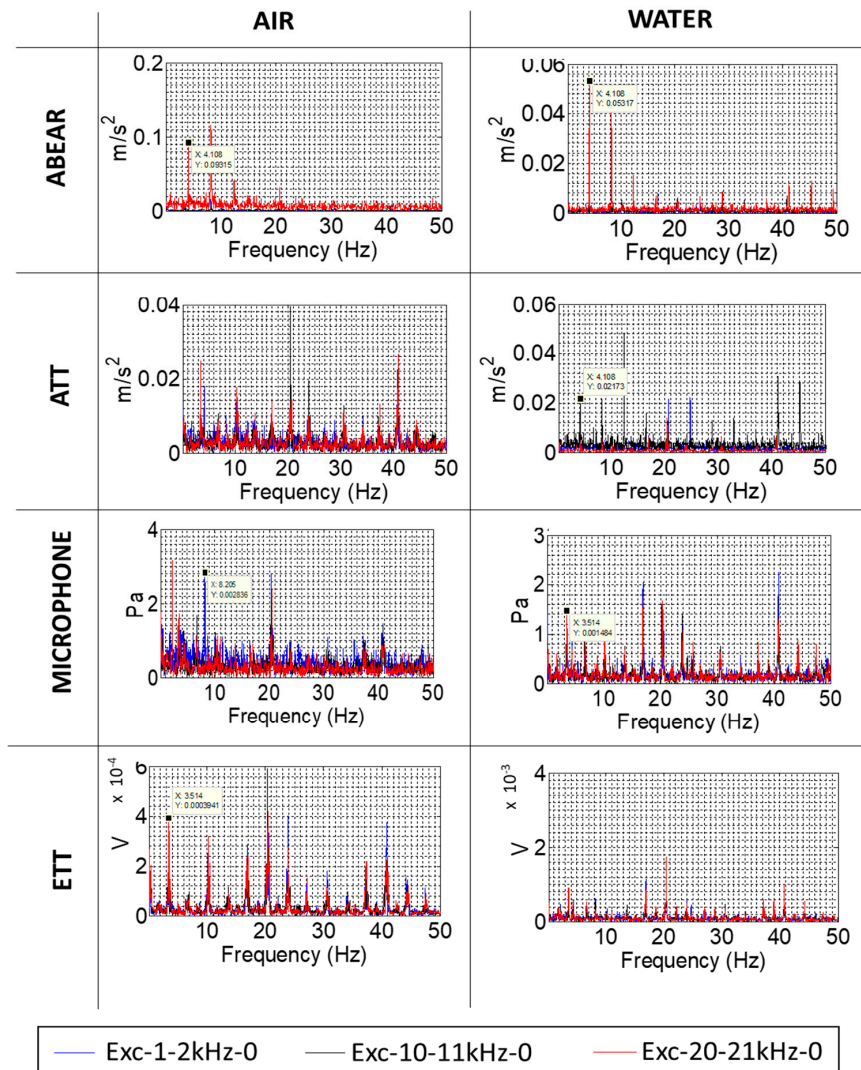


Figure 8. Amplitude demodulation for the sensors on the stationary frame and the excitation without any modulating frequencies. Rotating case ($f_f = 4.1$ Hz).

3.3.2. With One Modulating Frequency

The results presented in this section are the ones obtained with the excitations called “Exc-1-2kHz-1”, “Exc-10-11kHz-1”, and “Exc-20-21kHz-1” in Table 1. With the modulating frequency of $f_1 = 22.1$ Hz and the pseudorandom excitation, after an amplitude demodulation analysis, the frequencies expected to be found are the rotating frequency (f_f) for those cases under rotation, as in the previous case commented in Section 3.3.1., and the modulating frequency $f_1 = 22.1$ Hz.

Figure 9 shows the results for the rotating sensors as well for the PZT. The results for the PZT give the information of the excitation for the different excitation patterns. The amplitude of the modulating frequency f_1 is higher for the lower frequency band tested. This fact is due to the PZT characteristics, which behave differently at different frequency bands. Comparing the AE sensor in the shaft (ESH) with the excitation (PZT), the results are almost the same, which confirms that the EA sensor in the shaft represents very well the excitation in the disk. The cases where the rotating frequency was not found have been zoomed around the f_f in Figure 9. The accelerometers in the disk (ADISK) and in the shaft (ASH) give the same information than without any modulating frequency for the rotating frequency (f_f), but adding the modulating frequency f_1 . In the case of the accelerometer of the disk (ADISK), this frequency (f_1) is better seen in the frequency band of 10–11 kHz, whereas in the shaft it

is better seen in the frequency band of 20–22 kHz. This is related to the frequency resonance of every accelerometer, which is different for this both cases.

The results for some stationary sensors are shown in Figure 10. In this figure the most relevant sensors for the detection of the f_1 modulating frequency are shown. It is observed that the accelerometer located in the bearing (ABEAR) presents similar results than the one located in the shaft (ASH in Figure 9). This observation was also pointed out in the analysis without any modulating frequency (Section 3.3.1). Again, the high-frequency band is better able to detect the modulating frequency f_1 . The accelerometer installed in the upper cover (ATT) does not detect the modulating frequency in air, since the transmission of the disk vibration without water is very poor for this sensor (this was also confirmed in the coherence Section 3.1). However, it is clearly detected in the configuration with water, and the results obtained are very similar to those obtained with the accelerometer installed in the disk (ADISK in Figure 9). For this kind of accelerometer, the band 10–11 kHz is the best to detect the modulating frequency f_1 . Moreover, the microphone does not detect the modulating frequency f_1 since it is mainly receiving the information of the motor rotating speed, as it was commented in Section 3.3.1. Again, the AE sensor located in the head cover presents the same results than the microphone, since it is detecting the acoustic waves transmitted by the motor more than the ones transmitted by the PZT.

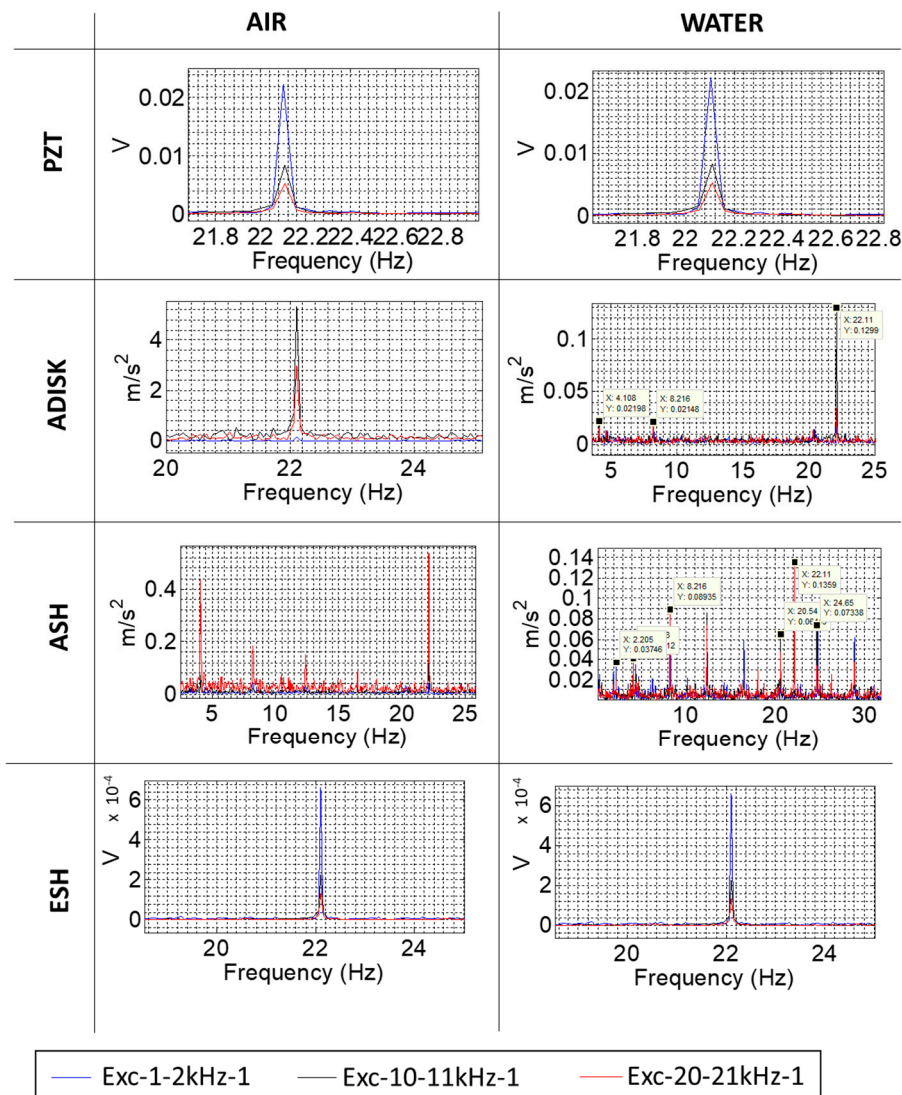


Figure 9. Amplitude demodulation for the sensors on the rotating frame and the excitation with one modulating frequency. Rotating case ($f_f = 4.1$ Hz).

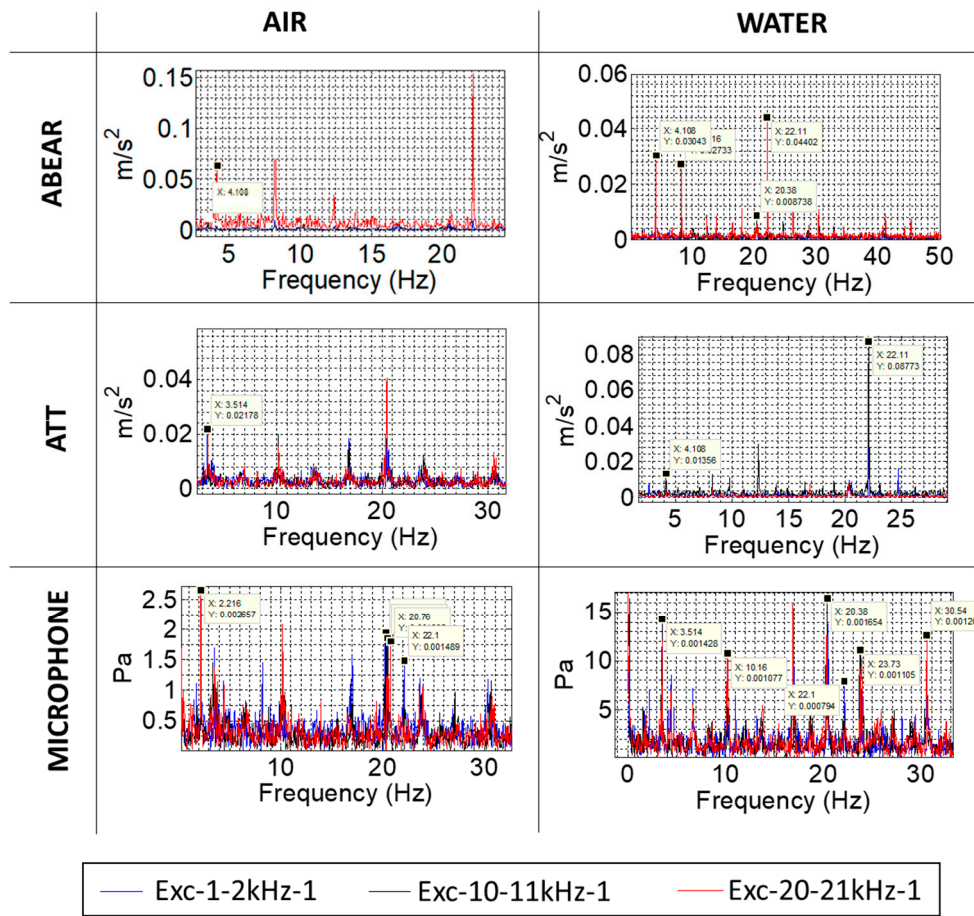


Figure 10. Amplitude demodulation for the sensors on the stationary frame and the excitation with one modulating frequency. Rotating case ($f_f = 4.1$ Hz).

3.3.3. With Two Modulating Frequencies

The results presented in this section are the ones obtained with the excitations called “Exc-1-2kHz-2”, “Exc-10-11kHz-2”, and “Exc-20-21kHz-2” in Table 1. With the modulating frequencies of $f_1 = 22.1$ Hz and $f_2 = 1.4$ Hz and the pseudorandom excitation, after an amplitude demodulation analysis, the frequencies expected to be found are the rotating frequency (f_f) for those cases under rotation, as in the previous case commented in Section 3.3.1, and the modulating frequencies $f_1 = 22.1$ Hz and $f_2 = 1.4$ Hz.

The results obtained for the analysis of the two modulating frequencies and the sensors of the rotating frame are shown in Figure 11. The conclusions here are almost the same than in the case of one modulating frequency: the AE sensor in the shaft (ESH) detects the excitation and not the response of the structure, the accelerometer of the disk (ADISK) detects both modulating frequencies but better in the range of 10–11 kHz, and the accelerometer of the shaft (ASH) is affected by vibrations induced by the motor when water is considered, and it detects the modulating frequencies better at 20–21 kHz. The main difference between one and two modulating frequencies is that near the f_1 modulating frequency appear two other frequencies which correspond to $f_1 - f_2$ and $f_1 + f_2$, respectively. This has to be considered when analyzing complex systems with more than one modulating frequency, as in the case of a hydraulic turbine.

The results for the stationary sensors are plotted in Figure 12. Again, the same conclusions than in the case of one modulating frequency can be extracted with this results, but with the difference that the f_2 modulating frequency can also be observed as a difference between f_1 and the nearby peaks.

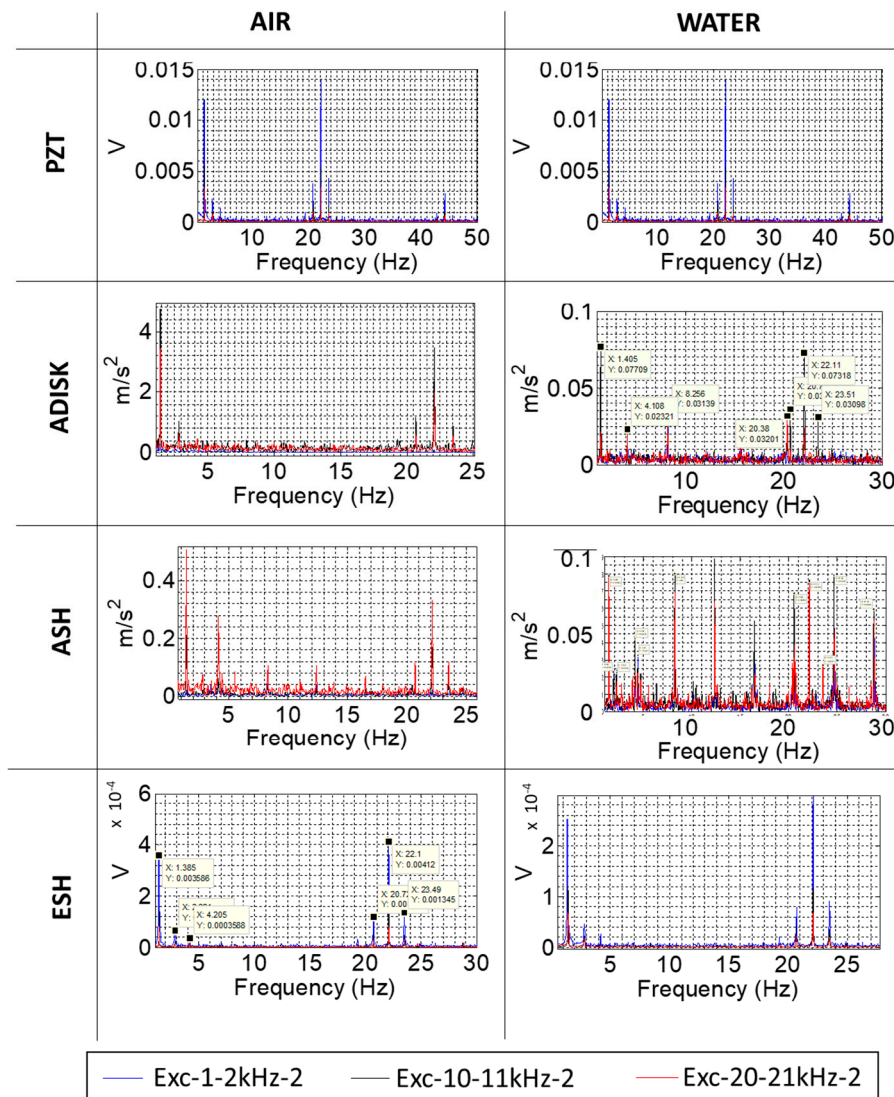


Figure 11. Amplitude demodulation for the sensors on the rotating frame and the excitation with two modulating frequencies. Rotating case ($f_f = 4.1$ Hz).

The microphone, as well as the AE sensor located in the upper cover, does not obtain the modulating frequencies f_1 and f_2 , but it detects vibrations induced by the motor. This means that the transmission of the acoustic waves through the air is stronger for the motor vibrations than for the disk vibrations.

The accelerometer located in the upper cover (ATT) again detects similar information than the one installed in the disk (ADISK) when there is water, which confirms that the transmission disk-cover is due mainly to the water. This accelerometer senses the modulating frequencies better in the 10–11 kHz band, which confirms that every kind of accelerometer and every position in the test rig has its own best high-frequency band to detect low-frequency phenomena by means of amplitude demodulation techniques.

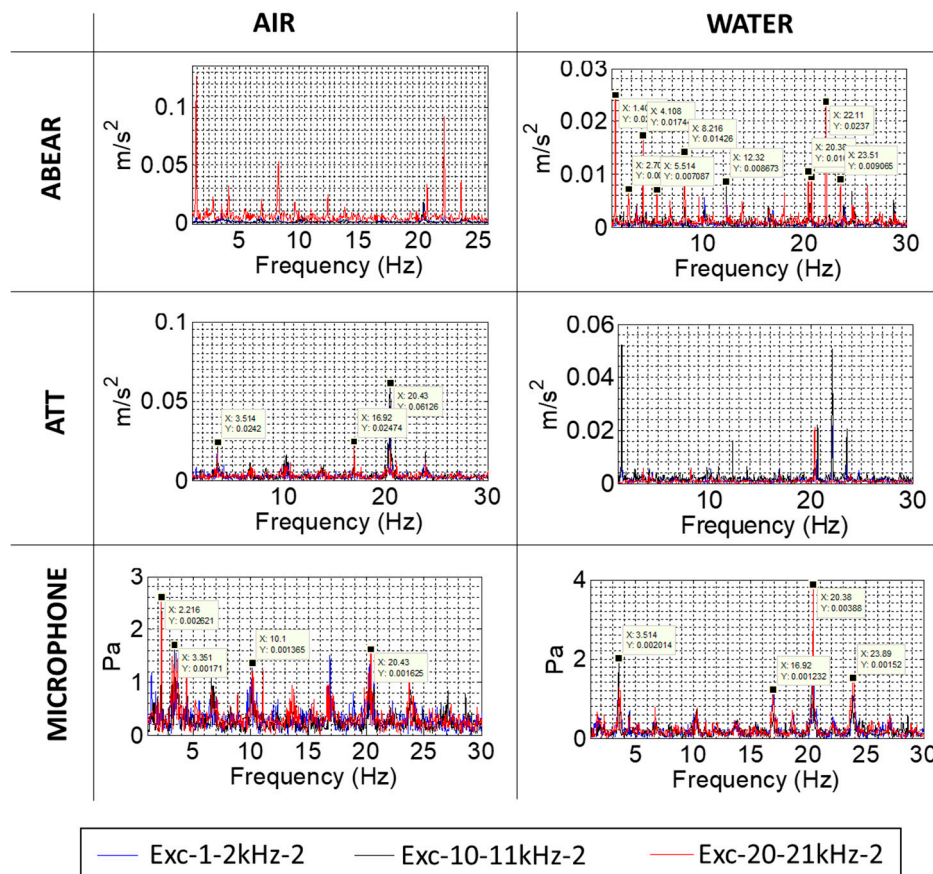


Figure 12. Amplitude demodulation for the sensors on the stationary frame and the excitation with two modulating frequencies. Rotating case ($f_f = 4.1$ Hz).

4. Conclusions

In this paper, the current method to detect erosive cavitation in hydraulic turbines by analyzing high-frequency vibrations has been revised by studying its main existing uncertainties. This method is based on measuring high-frequency vibrations provoked by the collapse of cloud cavitation bubbles near the runner in different parts of the machine. It compares RMS values and amplitude demodulation of different high-frequency bands and different sensors. However, the transmission path from the runner to the measuring points is not known when the machine is under operating conditions, as there is no visual correlation of cavitation and the measured signals, and it is still not clear which high-frequency bands have to be used for every sensor located in every position of the machine.

To optimize this current method, a simplified test rig based on a rotating disk submerged in water has been used. The disk has been excited with a PZT reproducing the excitation patterns caused by erosive cavitation, hence, the phenomenon of cavitation is not present in the test rig. Several sensors, including accelerometers, AE sensors, and a microphone, have been installed in the rotating and stationary parts of this test rig. This way, the excitation is completely known and, therefore, the transmission path between the excitation and the measuring point is obtained for every sensor. Different high-frequency bands have also been tested to study which are the best to detect the excitation for the different sensors. Thus, the best sensor and position to measure the given excitation is obtained.

The results obtained show that the sensors installed in the rotating frame are the best to detect the excitation at high-frequency given to the disk. Especially, the AE sensor installed in the shaft was the best sensor to detect the excitation, since it is able to eliminate the structural response of the shaft and only obtain the information of the excitation, for all kinds of frequency bands tested. Accelerometers located in the shaft and in the disk detect both excitation and structural response, which can be

distinguished using the amplitude demodulation analysis. For these sensors, the excitation is better transmitted at high frequency (10 to 11 kHz or 20 to 21 kHz).

For the sensors installed in the stationary part, it has been demonstrated that the transmission of the disk vibration was better when the disk was submerged in water than in the case of the disk in air. This means that the disk vibration is mainly transmitted through the water. The accelerometer in the bearing presents similar results than the one located in the shaft, and the accelerometer in the upper cover shows relevant information also obtained by the accelerometer in the disk. The microphone and AE sensor located in the stationary frame are contaminated by the vibration of the motor and, in this case, they are not very useful to obtain the excitation in the disk.

The comparison made in the present study permits improving the current method to detect cavitation in hydraulic turbines. In this case, the best position and sensor have been selected as an AE sensor in the shaft, which works properly in both low- and high-frequency bands.

Acknowledgments: The authors would like to acknowledge the HYPERBOLE research project, granted by the European Commission (ERC/FP7-ENERGY-2013-1-Grant 608532) for the economic support received. We would also like to thank Voith Hydro[®] for helping to design, economically and technically, the test rig.

Author Contributions: Alexandre Presas, David Valentin, Eduard Egusquiza, and Carme Valero conceived and designed the experiments; Alexandre Presas performed the experiments; Alexandre Presas, David Valentin, and Mònica Egusquiza analyzed the data; and David Valentin wrote the paper.

Conflicts of Interest: The authors declare no conflict of interest.

Nomenclature

AE	Acoustic Emission
BEP	Best Efficiency Point
RMS	Root Mean Square
RSI	Rotor Stator Interaction
PS	Pseudorandom
PZT	Piezoelectric Patch
f	Frequency
t	Time
H_i	Hilbert transform
θ	Phase shift
f_f	Rotating frequency
f_1	Modulating frequency at 22.1 Hz
f_2	Modulating frequency at 1.4 Hz
FRF_{H1}	Frequency Response Function
$S_{xx}(f)$	Power Spectra Density function of $x(t)$
$S_{yy}(f)$	Power Spectra Density function of $y(t)$
$S_{xy}(f)$	Cross-spectral Density function of $x(t)$ and $y(t)$
τ	Variable which satisfies $\tau \neq t$

References

1. Bélanger, C.; Gagnon, L. Adding wind energy to hydropower. *Energy Policy* **2002**, *30*, 1279–1284. [CrossRef]
2. IEA (International Energy Agency). Key World Energy Trends. Excerpt from: World Energy Balances. 2016. Available online: www.iea.org (accessed on 10 November 2017).
3. Gaudard, L.; Romero, F. The future of hydropower in Europe: Interconnecting climate, markets and policies. *Environ. Sci. Policy* **2014**, *37* (Suppl. C), 172–181. [CrossRef]
4. Egusquiza, E.; Valero, C.; Huang, X.; Jou, E.; Guardo, A.; Rodriguez, C. Failure investigation of a large pump-turbine runner. *Eng. Failure Anal.* **2012**, *23*, 27–34. [CrossRef]
5. Egusquiza, E.; Valero, C.; Presas, A.; Huang, X.; Guardo, A.; Seidel, U. Analysis of the dynamic response of pump-turbine impellers. Influence of the rotor. *Mech. Syst. Signal Process.* **2016**, *68–69*, 330–341. [CrossRef]

6. Trivedi, C. A review on fluid structure interaction in hydraulic turbines: A focus on hydrodynamic damping. *Eng. Failure Anal.* **2017**, *77*, 1–22. [[CrossRef](#)]
7. Frosina, E.; Buono, D.; Senatore, A. A Performance Prediction Method for Pumps as Turbines (PAT) Using a Computational Fluid Dynamics (CFD) Modeling Approach. *Energies* **2017**, *10*, 103. [[CrossRef](#)]
8. Kumar, P.; Saini, R.P. Study of cavitation in hydro turbines—A review. *Renew. Sustain. Energy Rev.* **2010**, *14*, 374–383. [[CrossRef](#)]
9. Escaler, X.; Eguisquiza, E.; Farhat, M.; Avellan, F.; Coussirat, M. Detection of cavitation in hydraulic turbines. *Mech. Syst. Signal Process.* **2006**, *20*, 983–1007. [[CrossRef](#)]
10. Knapp, R.; Daily, J.; Hammit, F. *Cavitation*; McGraw-Hill: New York, NY, USA, 1970; Volume 2, pp. 1–20.
11. Avellan, F.; Farhat, M. *Shock Pressure Generated by Cavitation Vortex Collapse*. ASME, San Francisco, December 1988, *Proceedings of 3rd International Symposium on Cavitation Noise and Erosion in Fluid System of the ASME Winter Annual Meeting, San Francisco, CA, USA, December 1989*; EPFL Scientific Publications: Lausanne, Schweizerische; pp. 119–125.
12. Favrel, A.; Müller, A.; Landry, C.; Yamamoto, K.; Avellan, F. Study of the vortex-induced pressure excitation source in a Francis turbine draft tube by particle image velocimetry. *Exp. Fluids* **2015**, *56*, 215. [[CrossRef](#)]
13. Favrel, A.; Müller, A.; Landry, C.; Gomes, J.; Yamamoto, K.; Avellan, F. *Dynamics of the Precessing Vortex Rope and Its Interaction with the System at Francis Turbines Part Load Operating Conditions*; Journal of Physics: Conference Series, 2017; IOP Publishing: Bristol, UK, 2017; p. 012023.
14. Müller, A.; Favrel, A.; Landry, C.; Avellan, F. Fluid–structure interaction mechanisms leading to dangerous power swings in Francis turbines at full load. *J. Fluids Struct.* **2017**, *69* (Suppl. C), 56–71. [[CrossRef](#)]
15. Yamamoto, K.; Müller, A.; Favrel, A.; Landry, C.; Avellan, F. *Flow Characteristics and Influence Associated with Inter-Blade Cavitation Vortices at Deep Part Load Operations of a Francis Turbine*; Journal of Physics: Conference Series, 2017; IOP Publishing: Bristol, UK, 2017; p. 012029.
16. Avellan, F.; Dupont, P.; Ryhming, I.L. *Generation Mechanism and Dynamics of Cavitation Vortices Downstream of a Fixed Leading Edge Cavity*, *Proceedings of the 17th Symposium on Naval Hydrodynamics, The Hague, The Netherlands, 28 August–2 September 1988*; EPFL Scientific Publications: Lausanne, Schweizerische; pp. 1–13.
17. Escaler, X.; Ekanger, J.V.; Francke, H.H.; Kjeldsen, M.; Nielsen, T.K. Detection of Draft Tube Surge and Erosive Blade Cavitation in a Full-Scale Francis Turbine. *J. Fluids Eng.* **2014**, *137*, 011103. [[CrossRef](#)]
18. Escaler, X.; Farhat, M.; Ausoni, P.; Eguisquiza, E.; François, A. *Cavitation Monitoring of Hydroturbines: Tests in a Francis Turbine Model*; CAV2006: Wageningen, The Netherlands, 2006.
19. Bajic, B. Multidimensional diagnostics of turbine cavitation. *J. Fluids Eng.* **2002**, *124*, 943–950. [[CrossRef](#)]
20. Bajić, B.; Keller, A. Spectrum Normalization Method in Vibro-Acoustical Diagnostic Measurements of Hydroturbine Cavitation. *J. Fluids Eng.* **1996**, *118*, 756–761. [[CrossRef](#)]
21. Escaler, X.; Eguisquiza, E.; Farhat, M.; Avellan, F. Vibration Cavitation Detection Using Onboard Measurements. In *Proceedings of the Fifth International Symposium on Cavitation*, Osaka, Japan, 1–5 November 2003.
22. Cencič, T.; Hočevar, M.; Širok, B. Study of Cavitation in Pump-Storage Hydro Power Plant Prototype. In *Proceedings of the 6th IAHR International Meeting of the Workgroup on Cavitation and Dynamic Problems in Hydraulic Machinery and Systems*, Ljubljana, Slovenia, 9–11 September 2015.
23. Bourdon, P.; Simoneau, R.; Lavigne, P. *A vibratory Approach to the Detection of Erosive Cavitation*, *Proceedings of the ASME International Symposium on Cavitation Noise and Erosion in Fluid Systems, San Francisco, CA, USA, December 1989*; FED: Washington, DC, USA, 1989.
24. Vizmanos, C.; Eguisquiza, E.; Jou, E. Cavitation detection in a Francis turbine. *Int. J. Hydropower Dams* **1996**, *3*, 161–168.
25. Escaler, X.; Farhat, M.; Eguisquiza, E.; Avellan, F. Dynamics and Intensity of Erosive Partial Cavitation. *J. Fluids Eng.* **2007**, *129*, 886–893. [[CrossRef](#)]
26. Presas, A.; Eguisquiza, E.; Valero, C.; Valentin, D.; Seidel, U. Feasibility of Using PZT Actuators to Study the Dynamic Behavior of a Rotating Disk due to Rotor-Stator Interaction. *Sensors* **2014**, *14*, 11919–11942. [[CrossRef](#)] [[PubMed](#)]
27. Presas, A.; Valentin, D.; Eguisquiza, E.; Valero, C.; Seidel, U. Influence of the rotation on the natural frequencies of a submerged-confined disk in water. *J. Sound Vib.* **2015**, *337*, 161–180. [[CrossRef](#)]

28. Presas, A.; Valentin, D.; Egusquiza, E.; Valero, C.; Seidel, U. On the detection of natural frequencies and mode shapes of submerged rotating disk-like structures from the casing. *Mech. Syst. Signal Process.* **2015**, *60–61*, 547–570. [[CrossRef](#)]
29. Valentin, D.; Presas, A.; Egusquiza, E.; Valero, C. On the Capability of Structural–Acoustical Fluid–Structure Interaction Simulations to Predict Natural Frequencies of Rotating Disklike Structures Submerged in a Heavy Fluid. *J. Vib. Acoust.* **2016**, *138*, 034502. [[CrossRef](#)]
30. Presas, A.; Valentin, D.; Egusquiza, E.; Valero, C.; Egusquiza, M.; Bossio, M. Accurate Determination of the Frequency Response Function of Submerged and Confined Structures by Using PZT-Patches. *Sensors* **2017**, *17*, 660. [[CrossRef](#)] [[PubMed](#)]
31. Rodriguez, C.G.; Mateos-Prieto, B.; Egusquiza, E. Monitoring of Rotor-Stator Interaction in Pump-Turbine Using Vibrations Measured with On-Board Sensors Rotating with Shaft. *Shock Vib.* **2014**, *2014*, 8. [[CrossRef](#)]
32. Egusquiza, E.; Valero, C.; Valentin, D.; Presas, A.; Rodriguez, C.G. Condition monitoring of pump-turbines. New challenges. *Measurement* **2015**, *67*, 151–163. [[CrossRef](#)]
33. Presas, A.; Valentin, D.; Egusquiza, E.; Valero, C.; Seidel, U. Experimental analysis of the dynamic behavior of a rotating disk submerged in water. *IOP Conf. Ser. Earth Environ. Sci.* **2014**, *22*, 032043. [[CrossRef](#)]
34. Presas, A.; Valentin, D.; Egusquiza, E.; Valero, C.; Seidel, U. Dynamic response of a rotating disk submerged and confined. Influence of the axial gap. *J. Fluids Struct.* **2016**, *62*, 332–349. [[CrossRef](#)]
35. Presas, A.; Valentin, D.; Egusquiza, E.; Valero, C.; Seidel, U.; Weber, W. *Natural Frequencies of Rotating Disk-Like Structures Submerged Viewed from the Stationary Frame*; IOP Conference Series: Earth and Environmental Science, 2016; IOP Publishing: Bristol, UK, 2016; p. 082023.
36. Heylen, W.; Sas, P. *Modal Analysis Theory and Testing*; Katholieke Universteit Leuven, Departement Werktuigkunde: Leuven, Belgium, 2006.



© 2018 by the authors. Licensee MDPI, Basel, Switzerland. This article is an open access article distributed under the terms and conditions of the Creative Commons Attribution (CC BY) license (<http://creativecommons.org/licenses/by/4.0/>).